IEEE Photonics Journal
An IEEE Photonics Society Publication

Open Access

In-Line Hybrid Fiber Sensor for Curvature and Temperature Measurement

Volume 11, Number 6, December 2019

Haihao Cheng
Shun Wu
Qiang Wang
Shun Wang
Peixiang Lu

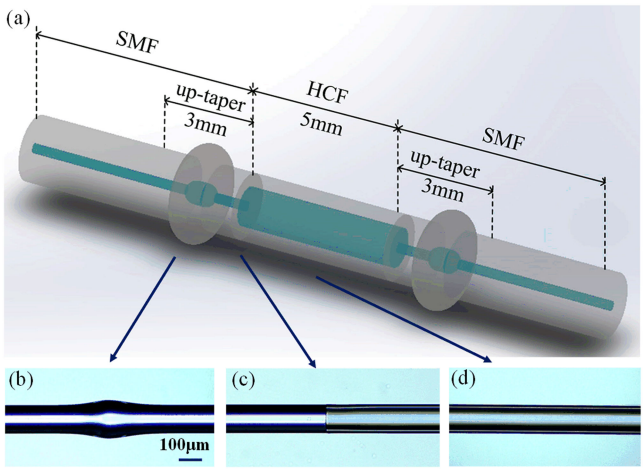

DOI: 10.1109/JPHOT.2019.2944988

IEEE photonics SOCIETY
IEEE

In-Line Hybrid Fiber Sensor for Curvature and Temperature Measurement

Haihao Cheng,[1] Shun Wu,[1] Qiang Wang,[1] Shun Wang,[1] and Peixiang Lu[1,2]

[1]Hubei Key Laboratory of Optical information and Pattern Recognition, Wuhan Institute of Technology, Wuhan 430205, China
[2]School of Physics and Wuhan National Laboratory for Optoelectronics, Huazhong University of Science and Technology, Wuhan 430074, China

DOI:10.1109/JPHOT.2019.2944988

Manuscript received September 2, 2019; revised September 22, 2019; accepted September 28, 2019. Date of publication October 2, 2019; date of current version November 11, 2019. This work was supported by the National Natural Science Foundation of China (NSFC) under Grant 61805182. Corresponding author: Shun Wu (e-mail: wushun@wit.edu.cn).

Abstract: We proposed and demonstrated a compact inline optical fiber sensor for curvature and temperature measurement with low cross sensitivity. The device consists of a 5 mm long hollow-core fiber (HCF) spliced between two single-mode fibers. Two up-tapers were fabricated at each splicing joint forming a Mach-Zehnder Interferometer (MZI). The HCF acted as the anti-resonant reflecting optical waveguide (ARROW), giving periodic dips at resonant wavelengths in the optical transmission spectrum. The cross sensitivity of curvature and temperature problem is solved by demodulating the wavelength shift of the MZI for temperature sensing and intensity variation of ARROW dips for curvature sensing. The curvature and temperature sensitivities are experimentally measured to be -4.28 dB/m^{-1} and 25.76 pm/°C, respectively. The cross sensitivities for ARROW is measured to be 0.0056 m^{-1}/°C. The structure of the sensor is simple and compact, which can be used for structural health monitoring in a complex environment.

Index Terms: Dual-parameter sensor, Curvature sensor, Temperature sensor, Mach-Zehnder interferometer, Anti-resonant reflecting.

1. Introduction

Optical fiber sensors have been extensively studied due to their intrinsic advantages of light weight, small size, flexibility, and immunity to electromagnetic interference. Among the various physical parameters, curvature plays an important role in structural health monitoring, robotic arms, automotive industry, and other mechanical engineering areas. To date, a variety of optical fiber structures have been developed for curvature measurement, for example, fiber grating-based [1], interferometer-based [2]–[12], anti-resonant-reflecting-guidance based [13] schemes. In the category of in-line interferometer-based curvature sensors, Mach-Zehnder interferometer (MZI) is an attractive configuration due to its merits of compact structure, high sensitivity and wavelength encoded detection with high reproducibility. The MZI is usually formed by splitting and later recombining different optical modes, i.e., core mode and cladding modes, at two separate fiber mode-coupling joints. The mode-coupling joints can be produced by fiber taper [4], [9], [14], dual-core fiber [15], lateral-offset splicing [16], or photonic crystal fiber collapsing [12]. Among these techniques, fiber taper is a favorable option because of its low cost and ease of operation with high reproducibility. Common taper

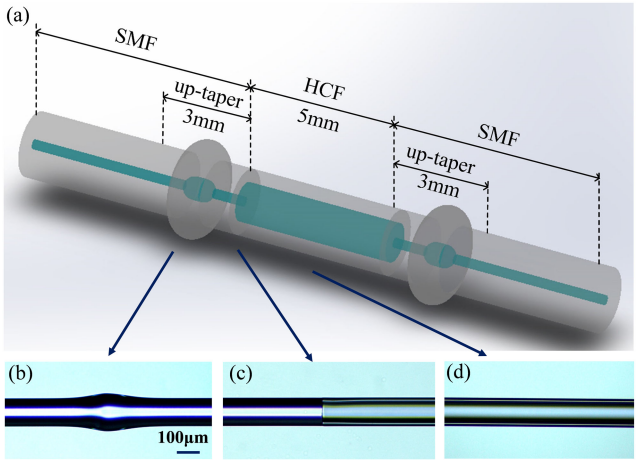

Fig. 1. (a) Schematics of our sensor structure. Microscopic images of (b) a SMF up-taper, (c) the splice between SMF to HCF, and (d) the HCF segment.

methods for curvature sensing are down-tapers and up-tapers forming peanut-shape or spherical-shape structures [9], [11], [14].

Although MZI has benefits of high-precision, for curvature measurement, temperature cross-talk is a significant issue. A common strategy to avoid cross-talk is to measure curvature by examining different interference peaks [6], which have different response behavior to curvature and temperature. An alternate approach is to use different sensing mechanism for temperature and curvature. Some structures are reported, such as three-core fiber [17], two-core fibers (TCF) [18], seven-core fiber [19], LPFG [20]. However, these special fibers increases the fabrication complexity and the cost of the sensor system.

Recently, we reported a curvature sensor based on anti-resonant reflecting optical guidance (ARROW) [13]. ARROW is a phenomenon that when light enters the hollow core of a silica tube, it cannot be confined in the hollow core due to the lower refractive index of air compared to the ring-shape silica cladding. As a result, light propagates into the cladding. The inner and outer side of the ring cladding form a Fabry-Perot cavity. When the wavelength of the light satisfies the resonant condition of the cavity, light will not be reflected inside the cavity any more, but leak out of the cladding instead, resulting in the periodic attenuation dips in the transmission spectrum [21]. By measuring the transmission power of the resonant dips for various bending curvature, we obtained a high sensitivity of -15.33 dB/m^{-1} in the range of 3.63 to 4.69 m^{-1} [13].

Based on our previous work of curvature sensor [13], we move a step forward towards the goal of realizing dual-parameter measurement of curvature and temperature with low cross-sensitivity. In this paper, we proposed and demonstrated a novel configuration for an optical fiber sensor based on a hybrid structure of MZI and ARROW. The MZI is formed by two up-tapers of single mode fiber. With a short segment of glass capillary sandwiched between the two up-tapers, an ARROW structure is formed. The bending of the sensor induces a change in the resonant condition of ARROW, leading to a variation in the dip intensity. Since we are monitoring two different aspects of the transmission spectrum, i.e., wavelength shift and dip intensity, the temperature and curvature cross-sensitivity can be largely eliminated through this demodulation technique.

2. Sensor Fabrication

The proposed sensor structure is displayed in Fig. 1(a). It is fabricated by introducing a section of HCF sandwiched between two single-mode fiber (SMF) up-tapers. The SMF is purchased from YOFC, Ltd with core/cladding diameter 8/125 μm. HCF is a pure quartz capillary tube (CT),

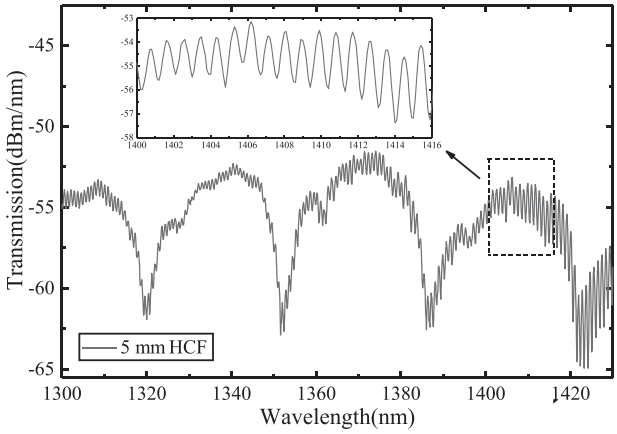

Fig. 2. Transmission spectrum of the hybrid sensor. Inset shows the magnified structure of the MZI interference fringes on top of the periodic ARROW attenuation dips.

purchased from Polymicro Technologies Ltd. It has a core diameter of 75 μm and the cladding diameter of 125 μm. We modified several parameters of the standard SM-SM splice recipe in a commercial fusion splicer (Fujikura FSM-80S) in order to produce the dumbbell structure of the SMF up-taper: the overlapping option was modified from standard value to 150 μm; The arc discharge intensity was set as $+10$ bit, with all other parameters remains unchanged. Once the discharge was finished, we repeated the above steps and made the second up-taper. Finally, we spliced the two SMF up-tapers to both ends of the HCF, one on each side. In this step, we followed the basic splicing parameters of the MM-MM mode to complete the fusion. The deformation of HCF can be caused by excessive heating. In order to avoid the collapse of the air hole, we carefully reduced the discharge power from the standard value to be -70 bit, shortened the discharge time to be 600 ms. The optimized overlap parameters was selected to be 10 μm. Fig. 1(b)–(d) shows the microscopic view of an up-taper, the splice between SMF and HCF, and a section of HCF. The waist diameter and length of the up-taper are measured to be 160.47 μm and 302.33 μm, respectively.

3. Principle of Hybrid Fiber Sensor

The first up-taper acts as a beam splitter. When light goes through the interface between SMF and up-taper, high order cladding modes will be excited due to mode field mismatch. The core mode and cladding modes continue to travel inside the HCF until they reach the second up-taper. The incoming beams are combined and part of the excited cladding modes are coupled back to the core of SMF. Due to the optical phase difference between the core mode and the excited cladding modes, a typical MZI is formed. In addition to the MZI interference pattern, a segment of HCF behaves as an ARROW which gives rise to a series of sharp lossy dips in the transmission spectrum. The spectral properties of the HCF waveguide can be understood as follows. HCF has an air-core, ring-shape glass cladding, and air again external to the cladding. It can be considered as a waveguide formed by a low-index core surrounded by a high-index cladding layer. The cladding acts as a Fabry-Perot (FP) resonator. When the wavelength of the light satisfies the resonance condition of the FP resonator, they will not be reflected by the FP etalon, but leak out of the cladding, resulting in transmission dips in the spectrum [22]. For wavelengths far from the resonance, the so-called anti-resonance region, light experiences low leakage due to destructive interference in the FP resonator, corresponding to high transmission bands in the spectrum.

The optical spectrum of the hybrid sensor is a combining result of both Mach-Zehnder interference and anti-resonance effect, as illustrated in Fig. 2. According to the optical interference theory, the

intensity for an interferometer can be express as:

$$I = I_{co} + I_{cl} + 2\sqrt{I_{co} \cdot I_{cl}}\cos\delta \tag{1}$$

where I_{co} and I_{cl} represent the intensities of the core mode and the higher-order cladding mode involved in the interference. The subscript "co" and "cl" denote for single mode fiber core and cladding, respectively. δ is the propagation phase shift in the interferometer. After propagating distance L, the accumulated phase difference δ between the two light paths is:

$$\delta = \frac{2\pi}{\lambda}(n_{co} - n_{cl})L = \frac{2\pi}{\lambda}\Delta n_{eff} L \tag{2}$$

Here, λ is the optical wavelength of the light source, L is the length of the MZI. Δn_{eff} is the difference between two refractive index n_{co} and n_{cl}, representing the birefringence between the core mode and the higher-order cladding mode. Since light propagates through a section of HCF, we modified Eqn (2) to:

$$\delta = \frac{2\pi}{\lambda}(n_{co} - n_{cl})L_1 + (n_{air} - n_{HCF})L_2 = \frac{2\pi}{\lambda}L_{OPD} \tag{3}$$

where L_1 and L_2 are the distances light travels inside SMF and HCF, respectively, between the two up-tapers. n_{air} and n_{HCF} represent the refractive index of the air core and silica cladding of the HCF. The subscript "OPD" denotes for optical path difference. A transmission dip will occur when the phase difference satisfies the resonant condition:

$$\delta = (2k + 1)\pi \tag{4}$$

Here, $(2k + 1)$ is the resonance order, and k is a positive integer. The wavelength for the MZI dip can be expressed as:

$$\lambda_{MZI} = \frac{2L_{OPD}}{2k + 1} \tag{5}$$

The distance between the two adjacent MZI dips (FSR) in the transmission spectrum can be written as:

$$FSR = \frac{\lambda^2}{L_{OPD}} \tag{6}$$

Regarding the anti-resonance effect, the anti-resonant wavelength λ_m can be expressed in terms of the cladding thickness d as follows, according to Ref. [22]:

$$\lambda_m = \frac{2d\sqrt{n_{HCF}^2 - 1}}{m} \tag{7}$$

Here, m is a positive integer representing the resonance order, n_{HCF} is the refractive index of silica. The intensity of the transmission fringes can be expressed as [21]:

$$T_{ARROW} = \frac{(1 - n_{air} \times n_{HCF})^2 (n_{air} + n_{HCF})^2}{1 + {n_{HCF}}^4 - 2{n_{HCF}}^2} I_{ARROW} \tag{8}$$

Here, n_{air} and n_{HCF} are the refractive index of the ring shape inner-core and outer-core cladding. I_{ARROW} is the intensity of the incident light at the resonant wavelength. We can see that the intensity of the resonant wavelength is influenced by the reflective coefficient at both boarders of F-P resonator.

When the external temperature changes, the refractive index of cladding mode will change, leading to a change in the difference of the optical phase between the core mode and the higher-order modes, and a shift of the MZI fringes is expected. However, considering the high thermo-optic coefficient of fused silica (1.2×10^{-5} [23]), and low thermal expansion coefficient of 5.5×10^{-7} /°C, temperature has a minor effect on the refractive Index and thickness of HCF, so the ARROW dip intensities is insensitive to temperature variation.

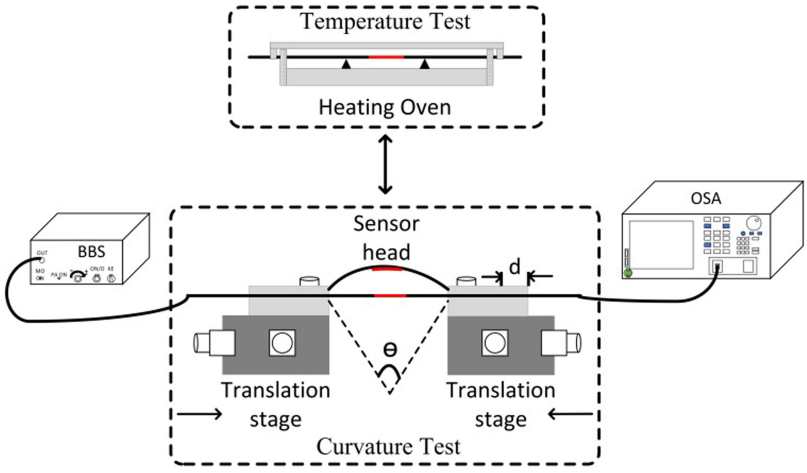

Fig. 3. Experimental setup for measuring temperature (upper dash box) and curvature (lower dash box) of the proposed sensor. Red lines indicate the 12 mm sensor head, with two SMF up-tapers and a segment of 5 mm HCF. BBS: broadband light source, OSA: optical spectrum analyzer.

In the case of curvature change, the silica capillary is compressed on one side while stretched on the other side. This has two consequences. On one hand, the core mode and cladding mode involved for interference propagate asymmetrically around the capillary. As a result, the path length difference for MZI varies under different bending conditions. Therefore, the wavelength of the MZI transmission dips shift accordingly. On the other hand, when bending occurs, the propagation symmetry of interference beam around the silica tube is destroyed: the spacing between the output interfering beams on the stretching side is increased, and the opposite on the compressed side. Considering the limited incident angle of the guide light, the intensity of the ARROW dips will change as curvature increases.

4. Experiment and Discussion

In our experiment, a broadband source (BBS, YSL, 900 nm-1700 nm) is used as the light source, and an optical spectrum analyzer (OSA, YOKOGAWA AQ6370B) is utilized to measure the optical transmission spectrum, with a resolution of 20 pm. The transmission spectrum of the sensor is shown in the Fig. 2.

The large-spaced attenuation dips come from the anti-resonance leakage occurring at resonant wavelengths, while the inset shows the magnified MZI fringes. Fig. 3 shows the experimental setup for both temperature and curvature measurement, indicated by the upper and lower dash box.

We investigated the influence of the HCF length on the optical transmission spectrum. Fig. 4 shows the comparison of three different HCF lengths: 1.2 mm, 5 mm, and 10 mm. Our results showed that when the HCF is short, although the interference fringes have larger FSR with higher contrast, the anti-reflection effect becomes less prominent, indicated by the case when the HCF was chosen to be 1.2 mm (blue curve in Fig. 4). When the HCF is long, as in the 10 mm case (red curve in Fig. 4), FSR becomes smaller, giving a denser fringes but lower contrast. The reduction in fringe contrast is expected because it is largely dependent upon the power balance between the core modes and the excited higher order modes. The latter experiences higher loss as they travel inside the cladding over a longer distance, resulting in significantly reduced contrast for the 10 mm HCF.

In order to compromise clear ARROW dips and profound MZ interference fringes, we have chosen the length of the HCF segment to be 5 mm. The corresponding transmission spectrum is shown as

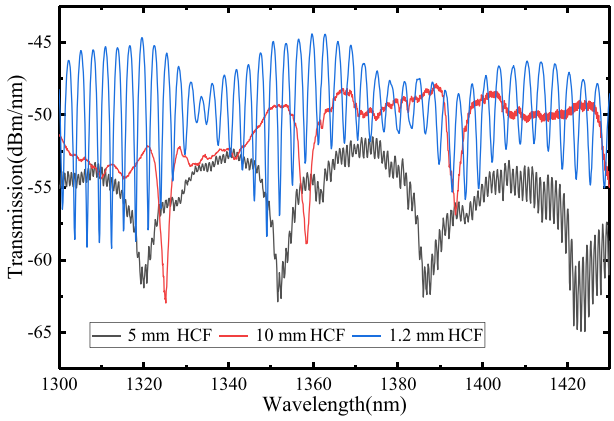

Fig. 4. Transmission spectrum for different length of HCF.

the black curve in Fig. 4. The total length of the hybrid structure including the two up-tapers was about 12 mm.

4.1 Curvature Measurement

For curvature measurement, as displayed in Fig. 3, the proposed hybrid structure sensor is placed between two translation stages, with each end fixed by a fiber holder on a translation stage. One stage is stationary, while the other stage is moved inward to bend the sensor region. When the fiber bends, it can be seen as an arc of a circle. The curvature can be obtained from the following equation:

$$R \sin \frac{L}{2R} = \frac{L - D}{2} \tag{9}$$

$$C = \frac{1}{R} \tag{10}$$

Here, L is the initial position, D is the displacement of the translation stage, R is the radius of curvature. Curvature is defined as the inverse of R. As we tune the micrometer of the movable translation stage, the curvature of the sensor changes, leading to a change in the optical transmission spectrum of the sensor. Fig. 5 and Fig. 6 investigate how the MZI and ARROW spectrum response to curvature change at room temperature of 23 °C, respectively.

When the sensor head is bent, the optical path difference (OPD) of the MZI changes, which leads to the wavelength shift of the dips. We found that this wavelength shift near 1388 nm at various curvatures shows a sensitivity of 49.9 pm/m^{-1}. Meanwhile, due to curvature change [13], the transmission intensity of the ARROW dip reduces as the curvature increases from 10.72 m^{-1} to 11.60 m^{-1}, as illustrated in Fig. 6(a). The sensitivity for intensity change is -4.28 dB/m^{-1} (Fig. 6(b)).

Because of the hybrid structure of MZI and ARROW, during curvature measurement, leakage of MZI modes occurs due to curvature change, leading to a slow intensity modulation due to MZI in the transmission spectrum. This in turn affects the ARROW dip intensity. To eliminate the intensity modulation in the ARROW spectrum due to the curvature variation, we introduced fast Fourier transform (FFT) algorithm to the transmission spectrum. Fig. 7 shows one example of the spatial frequency spectra corresponding to the MZI fringes in the original spectrum. We observed several weak modes in the spatial frequency spectra near 1.08911 nm^{-1}. The signal includes higher-order cladding modes excited by the up-tapers, as well as other cladding modes excited due to the curvature change. We filtered these spatial frequency component and thus eliminate the slow intensity modulation envelope due to curvature change on top of the ARROW spectrum.

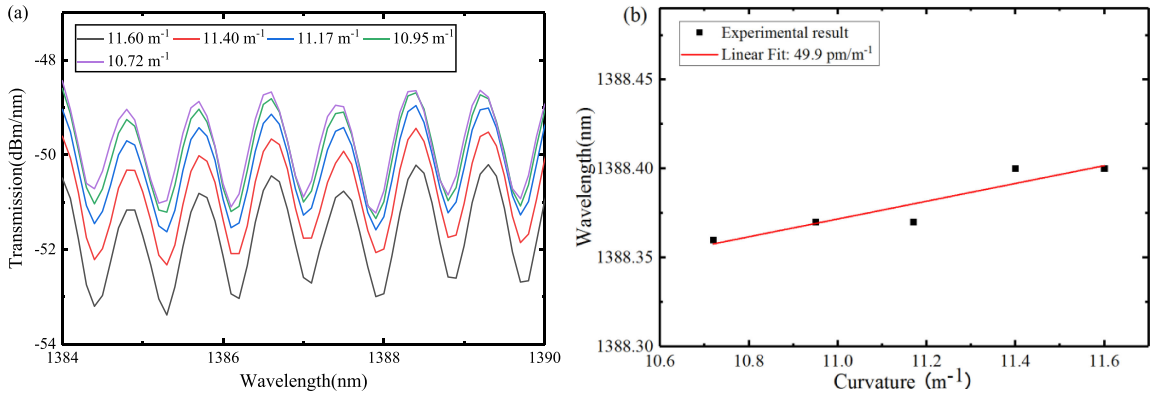

Fig. 5. (a) Optical transmission spectra near 1388 nm when the hybrid sensor was bent under various curvatures. This wavelength range was selected because the spectra around 1388 nm is least sensitive to curvature change. (b) The wavelength shift of the peak of a MZI fringe near 1388.3 nm at different curvatures. Linear fit (red line) indicates a curvature sensitivity of 49.9 pm/m^{-1}.

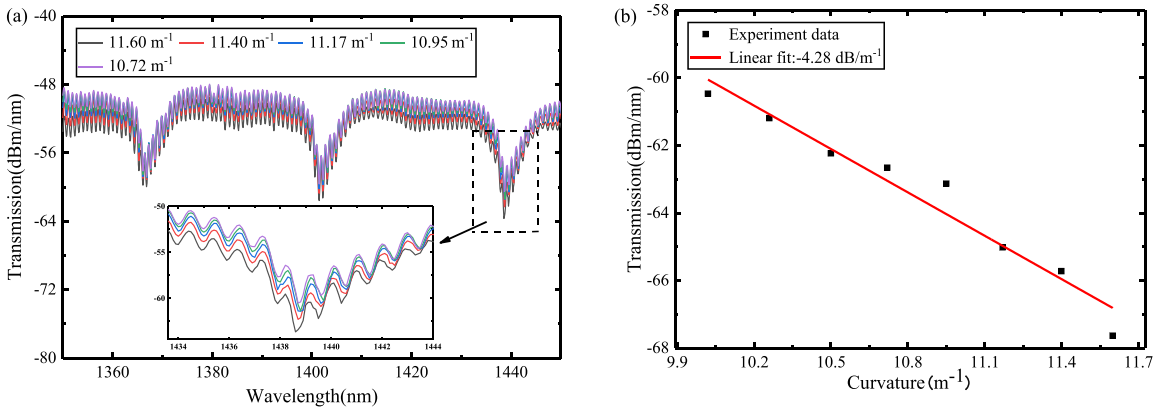

Fig. 6. (a) Schematic diagram of the transmission spectra when the hybrid sensor was bent with a curvature ranging from 10.72 m^{-1} to 11.60 m^{-1}. Inset: magnified spectrum of dip power variation near resonant wavelength 1438.6 nm. (b) The transmission intensity of the ARROW dip near 1438.6 nm. Linear fit for the intensity variation of ARROW dips as a function of curvature, indicating a curvature sensitivity of −4.28 dB/m^{-1}.

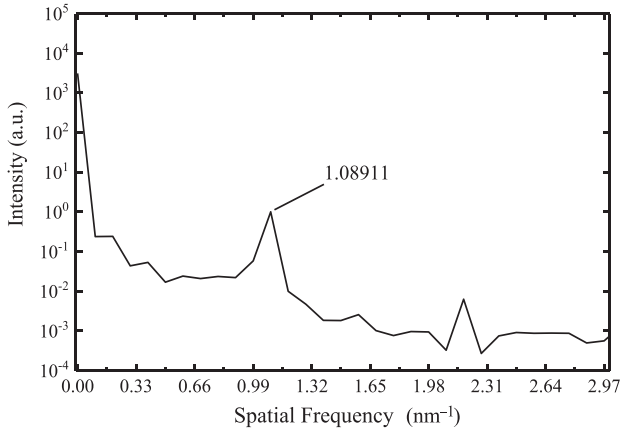

Fig. 7. Spatial frequency spectra of the sensor.

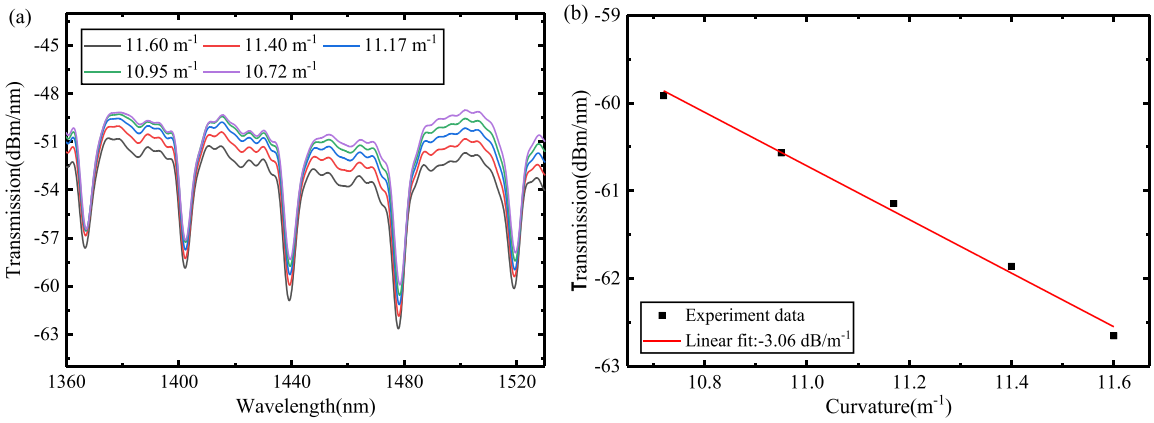

Fig. 8. Corrected data for (a) Fig. 6(a) and (b) Fig. 6(b) after filtering high spatial frequencies.

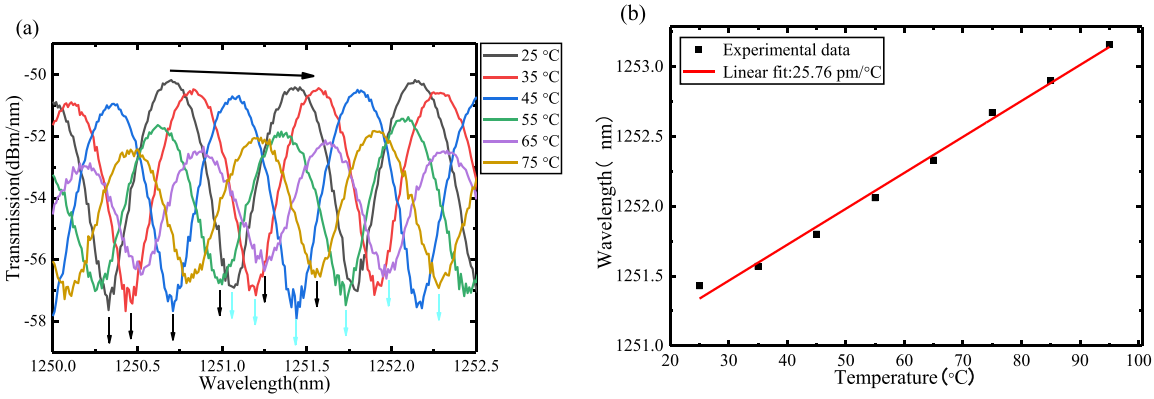

Fig. 9. (a) MZI spectra of the sensor at different temperatures. (b) Linear fit for the wavelength change of the MZI dips, indicating a temperature sensitivity of 25.76 pm/°C.

In this way, we obtained a more accurate sensitivity of -2.90 dB/m^{-1} at 1438.6 nm in the curvature measurement range of 10.72 to 11.60 m^{-1}. Fig. 8(a) shows the corrected ARROW spectrum after filtering the higher spatial frequency components. Compared with Fig. 6(a), the spectrum after filtering becomes cleaner. The corrected sensitivity of -3.06 dB/m^{-1} at 1479 nm in Fig. 8(b) has a higher linearity and is more accurate.

4.2 Temperature Measurement

For temperature measurement, the sensor head is placed inside an oven (ECOM, Column oven LCO 102 single). It is an enclosed box (44 $\times$ 47 $\times$ 325 mm) with a removable top. Inside the oven, there is a 32 cm-long V-groove, with a pair of metal clips at each end to clamp down a piece of fiber. The oven was tested before the experiment to make sure the entire sensor head was within the range for uniform heating inside the oven. The tuning range of the oven is from 25 °C to 90 °C, with an accuracy of 0.1 °C. As we change the temperature at steps of 10 °C, we recorded the transmission spectrum at six different temperatures, the black arrows and blue arrows indicate that the two wavelengths selected was drifted by temperature change as shown in Fig. 9(a). For each measurement, we waited until the temperature was steady before we moved on to the next measurement. As temperature increases, the MZI fringes experiences a red shift. Fig. 9(b) shows

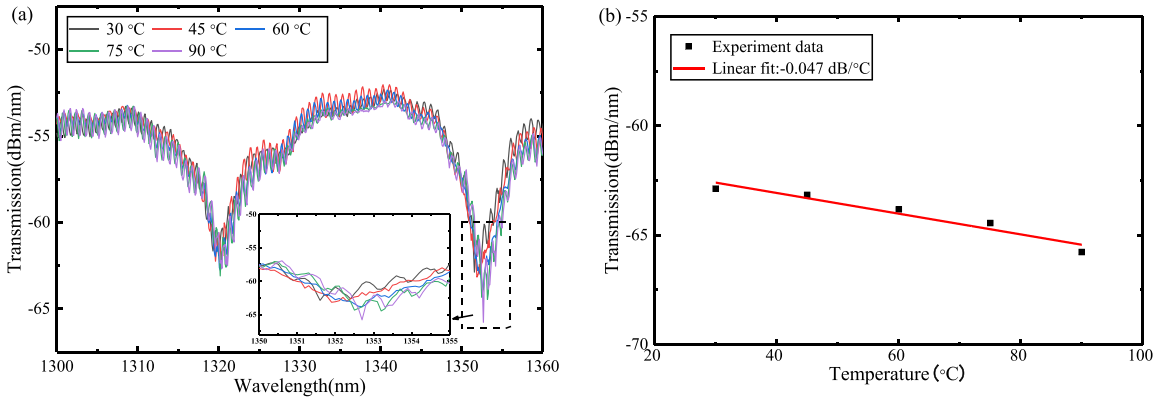

Fig. 10. (a) ARROW spectra of the sensor at different temperatures. Inset shows the magnified spectra at a resonant dip around 1353 nm. (b) The transmission intensity of the ARROW dip at 1353 nm. Linear fit for the intensity variation of ARROW dips as a function of temperatures, indicating a temperature sensitivity of 0.047 dB/°C.

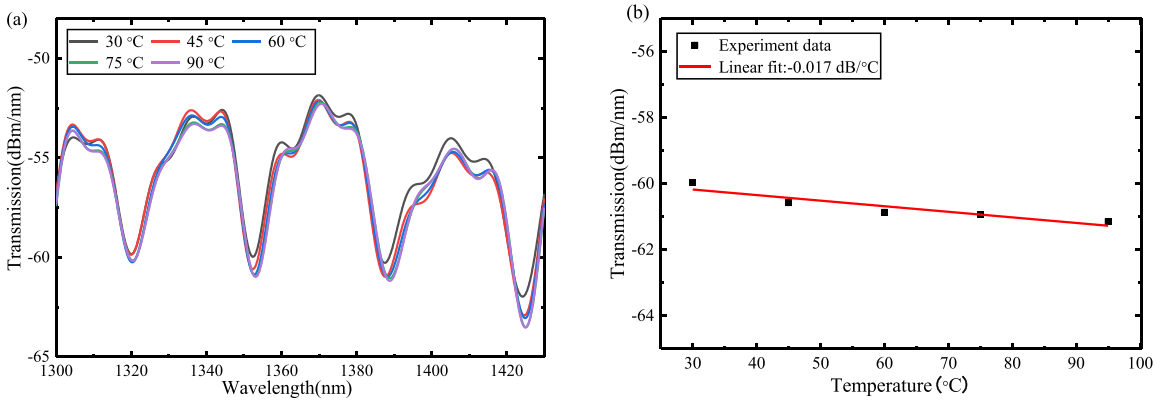

Fig. 11. Corrected data for (a) Fig. 10(a) and (b) Fig. 10(b) after filtering high spatial frequencies.

the wavelength shift of a MZI dip at eight different temperatures. The linear fit gives the temperature sensitivity of 25.76 pm/°C.

Meanwhile, we found that the temperature change has a minor effect on the ARROW dip intensity. Fig. 10(a) shows the transmission ARROW spectra at various temperature conditions. As we increase the oven temperature every 15 °C, the ARROW dip intensity at around 1353 nm slightly decreases. The linear fit of the dip intensity in Fig. 10(b) indicates that the temperature sensitivity of the ARROW intensity is −0.047 dB/°C.

In order to eliminate the intensity modulation effect of MZI caused by ambient temperature and bending curvature, and get a more accurate temperature measurement results from the ARROW spectrum, we performed similar FFT algorithm to the transmission spectrum to filter the high spatial mode using the data shown in Fig. 10. Fig. 11(a) shows the corrected spectrum. The curvature and temperature sensitivity was corrected to be -3.06 dB/m^{-1} and 0.017 dB/°C, as shown in Fig. 8(b) and 11(b). This indicates that temperature has a minor effect on the intensity of ARROW spectrum. More importantly, when using ARROW intensity for curvature measurement, the temperature cross sensitivity is as low as 0.0056 m^{-1}/°C.

The low temperature cross sensitivity demonstrated in our experiment is crucial to implement the curvature-temperature dual parameter measurement successfully. Since the ARROW dip intensity is caused mainly by the curvature change, the curvature change of the sensor can be determined

by monitoring the ARROW dip intensity change in the transmission spectrum. With the curvature change known, it is straightforward to determine the temperature change by monitoring the MZI wavelength shift. The total shift is contributed by both curvature and temperature change. After subtracting the contribution of the curvature from the overall shift, we can successfully calculate the unknown temperature, thus solving the cross-sensitivity problem.

5. Conclusions

In summary, we presented a novel inline optical fiber sensor for curvature and temperature measurement with low cross sensitivity. The device is compact, easy to fabricate and low cost. It consists of a 5 mm HCF sandwiched between a pair of symmetric up-tapers. In order to solve the cross sensitivity problem, our proposed scheme can decouple curvature and temperature by simultaneous detection of two independent parameters, i.e., the wavelength shift of MZI for temperature change, and intensity variation of ARROW dips for curvature change. The maximum sensitivities of intensity-curvature and wavelength-temperature relationships are -4.28 dB/m^{-1} (from 10.72 m^{-1} to 11.60 m^{-1}) and 25.76 pm/°C, respectively. By removing the high spatial frequency components in the ARROW spectrum, we eliminated the intensity modulation effect of MZI caused by ambient temperature and bending curvature, and obtained a more accurate curvature measurement of -3.06 dB/m^{-1} and temperature result of -0.017 dB/°C. The cross sensitivities for ARROW is 0.0056 m^{-1}/°C. Our device is also provided with many competitive advantages including ease of fabrication, high integration, and low cost. It can be a solution for dual-parameter measurement of temperature and curvature with low cross sensitivity. For future work, we will focus on filling materials with a high thermal-optic coefficient inside the HCF to further improve the temperature sensitivity.

References

[1] O. Frazão *et al.*, "All-fiber Mach–Zehnder curvature sensor based on multimode interference combined with a long-period grating," *Opt. Lett.*, vol. 32, no. 21, pp. 3074–3076, 2007.

[2] Y. Gong, T. Zhao, Y. J. Rao, and Y. Wu, "All-fiber curvature sensor based on multimode interference," *IEEE Photon. Technol. Lett.*, vol. 23, no. 11, pp. 679–681, Jun. 2011.

[3] R. Wang *et al.*, "Highly sensitive curvature sensor using an in-fiber Mach–Zehnder interferometer," *IEEE Sensors J.*, vol. 13, no. 5, pp. 1766–1770, May 2013.

[4] Q. Zeng, W. Xu, Y. Shen, C. Yu, and F. Tan, "Investigation on fiber optic curvature sensor based on SMF-FMF-SMF structure with up-taper fusion," *Proc. SPIE*, vol. 11048, 2019, Art. no. 110484A.

[5] S. Dong, B. Dong, C. Yu, and Y. Guo, "High sensitivity curvature sensor with a dual core photonic crystal fiber interferometer," in *Proc. 26th Int. Conf. Opt. Fiber Sensors*, Lausanne, Switzerland, 2018, Paper WF104.

[6] H. Gong, M. Xiong, Z. Qian, C. Zhao, and X. Dong, "Simultaneous measurement of curvature and temperature based on Mach–Zehnder interferometer comprising core-offset and spherical-shape structures," *IEEE Photon. J.*, vol. 8, no. 1, Feb. 2016, Art. no. 6800109.

[7] H. Gong, X. Yang, K. Ni, C. L. Zhao, and X. Dong, "An optical fiber curvature sensor based on two peanut-shape structures modal interferometer," *IEEE Photon. Technol. Lett.*, vol. 26, no. 1, pp. 22–24, Jan. 2014.

[8] S. Dong, D. Bo, C. Yu, and Y. X. Guo, "High sensitivity optical fiber curvature sensor based on cascaded fiber interferometer," *J. Lightw. Technol.*, vol. 36, no. 4, pp. 1125–1130, Feb. 2018.

[9] L. Mao, L. Ping, Z. Lao, and D. Liu, "Simultaneous measurement of curvature and temperature based on Mach–Zehnder interferometer with lateral offset and ultra-abrupt taper," in *Proc. Conf. Lasers Electro-Opt. Pacific Rim*, 2013, pp. 1–2.

[10] L. Mao, L. Ping, Z. Lao, D. Liu, and J. Zhang, "Highly sensitive curvature sensor based on single-mode fiber using core-offset splicing," *Opt. Laser Technol.*, vol. 57, no. 4, pp. 39–43, 2014.

[11] L. Niu, C. L. Zhao, H. Gong, Y. Li, and S. Jin, "Curvature sensor based on two cascading abrupt-tapers modal interferometer in single mode fiber," *Opt. Commun.*, vol. 333, pp. 11–15, 2014.

[12] H. Gong, H. Song, X. Li, J. Wang, and X. Dong, "An optical fiber curvature sensor based on photonic crystal fiber modal interferometer," *Sens. Actuators A, Phys.*, vol. 195, no. 6, pp. 139–141, 2013.

[13] S. Wang *et al.*, "An inline fiber curvature sensor based on anti-resonant reflecting guidance in silica tube," *Opt. Laser Technol.*, vol. 111, pp. 407–410, 2019.

[14] Z. Shanshan, Z. Weigang, G. Shecheng, G. Pengcheng, and X. Xiaolin, "Fiber-optic bending vector sensor based on Mach–Zehnder interferometer exploiting lateral-offset and up-taper," *Opt. Lett.*, vol. 37, no. 21, pp. 4480–4482, 2012.

[15] H. Qu., G. F. Yan, and M. Skorobogatiy, "Interferometric fiber-optic bending/nano-displacement sensor using plastic dual-core fiber," *Opt. Lett.*, vol. 39, no. 16, pp. 4835–4838, 2014.

[16] O. Zhilong *et al.*, "Ambient refractive index-independent bending vector sensor based on seven-core photonic crystal fiber using lateral offset splicing," *Opt. Exp.*, vol. 21, no. 20, pp. 23812–23821, 2013.

[17] L. Ding, Y. Li, C. Zhou, M. Hu, Y. Xiong, and Z. Zeng, "In-fiber Mach–Zehnder interferometer based on three-core fiber for measurement of directional bending," *Sensors*, vol. 19, no. 1, 2019, Art. no. 205.
[18] W. Yue *et al.*, "Highly sensitive curvature sensor based on asymmetrical twin core fiber and multimode fiber," *Opt. Laser Technol.*, vol. 92, pp. 74–79, 2017.
[19] H. Maoxiang *et al.*, "Two-dimensional vector bending sensor based on seven-core fiber Bragg gratings," *Opt. Exp.*, vol. 26, no. 18, pp. 23770–23781, 2018.
[20] C. Sun *et al.*, "A micro−MMF layer embedded in LPFG for simultaneous measurement of curvature and temperature," *Opt. Fiber Technol.*, vol. 48, pp. 134–137, 2019.
[21] S. Liu, T. Jie, N. Liu, J. Xia, and P. Lu, "Temperature insensitive liquid level sensor based on antiresonant reflecting guidance in silica tube," *J. Lightw. Technol.*, vol. 34, no. 22, pp. 5239–5243, Nov. 2016.
[22] S. Liu, T. Jie, S. Wang, W. Zhe, and P. Lu, "Anti-resonant reflecting guidance in silica tube for high temperature sensing," *IEEE Photon. Technol. Lett.*, vol. 29, no. 23, pp. 2135–2138, Dec. 2017.
[23] Z. Zhe *et al.*, "Hollow-core-fiber based interferometer for high-temperature measurements," *IEEE Photon. J.*, vol. 9, no. 2, pp. 1–9, Apr. 2017.